

Chemical Imaging Beyond the Diffraction Limit: Experimental Validation of the PTIR Technique **

Basudev Lahiri,^{1,2} Glenn Holland¹ and Andrea Centrone^{1,2}*

[*] Dr. Andrea Centrone, Dr. Basudev Lahiri,

¹NIST, Center for Nanoscale Science and Technology

Gaithersburg, 100 Bureau Drive, Stop 6204, MD 20899 (USA)

²University of Maryland, Institute for Research in Electronics and Applied Physics (IREAP),
College Park, MD 20742 (USA)

E-mail: Andrea.Centrone@nist.gov

Mr. Glenn Holland

¹NIST, Center for Nanoscale Science and Technology

Gaithersburg, 100 Bureau Drive, Stop 6204, MD 20899 (USA)

Supporting Information is available on the WWW under <http://www.small-journal.com> or from the author.

Keywords: Infrared Spectroscopy, Chemical Imaging, Nanoscale Characterization, AFM, Electron Beam Lithography

Abstract: Photo Thermal Induced Resonance (PTIR), recently attracted great interest for enabling chemical identification and imaging with nanoscale resolution. In this work, electron beam nano-patterned polymer samples are fabricated directly on 3-dimensional zinc selenide prisms and used to experimentally evaluate the PTIR lateral resolution, sensitivity and linearity. It is shown that PTIR lateral resolution for chemical imaging is comparable to the lateral resolution obtained in the AFM height images, up to the smallest feature measured (100 nm). Spectra and chemical maps were produced from the thinnest sample analyzed (40 nm). More importantly, experiments show for the first time that the PTIR signal increases linearly with thickness for samples up to $\approx 1 \mu\text{m}$ (linearity limit); a necessary requirement towards the use of the PTIR technique for quantitative chemical analysis at the nanoscale. Finally, the analysis of thicker samples provides the first evidence that the previously developed PTIR signal generation theory is correct. We believe that the findings of this work will foster nanotechnology development in disparate applications by proving the basis for quantitative chemical analysis with nanoscale resolution.

1. Introduction

Nanomaterials attract great interest owing to their novel size-dependent properties, allowing for improved performance over their macroscopic counterparts.^[1, 2] Investigation of nanomaterial's local properties (chemical, physical, etc.) as a function of location is a prerequisite for their advanced engineering and application in fields like electronics,^[3] photovoltaics,^[4] biology,^[5] and therapeutics.^[2, 6] Typically, nanomaterials are sequentially characterized at the nanoscale with multiple imaging or spectroscopic techniques that give morphological, structural or chemical information at different length scales and/or sample locations. For example, Fourier Transformed Infrared (FTIR) spectroscopy provides rich chemical and structural information,^[5, 7] but the diffraction of IR wavelengths (3 μm to 20 μm) limits the lateral resolution of FTIR microscopy to several micrometers.^[8]

To circumvent the limitations imposed by light diffraction few chemical imaging methods relying on scanning probe techniques have been proposed.^[9, 10, 11] In particular, scanning Near-field Optical Microscopy (s-SNOM)^[3, 9, 12] measures the light scattered by a sharp metallic tip when illuminated by a laser beam which induces an enhanced near field in proximity of the sample. s-SNOM proved to be successful in generating nanoscale IR images because the interaction of the near field IR radiation with the sample causes a change in the amplitude and phase of the scattered light as a function of the (local) index of refraction ($\tilde{n}(\lambda)$) given by:

$$\tilde{n}(\lambda) = n(\lambda) + i\kappa(\lambda) \quad (1)$$

where λ is the wavelength of light, n is the real part of the refractive index, and κ is the extinction coefficient. However, the interpretation of IR s-SNOM spectra relies on theoretical modeling^[13] which requires a description of the tip-sample-substrate interactions in the near field thus making the identification of unknown materials a challenging task. Since the s-SNOM scattered light depends on the tip-sample relative size^[12] and it is not a simple function

of κ , a more promising approach is relying on a technique sensitive to absorption instead of scattering.

Photothermal Induced Resonance (PTIR) is a new technique that combines the high lateral resolution of Atomic Force Microscopy (AFM) and the high chemical specificity of IR Spectroscopy.^[11, 14-17] PTIR spectra are obtained by measuring the instantaneous thermal expansion of the sample induced by the absorption a pulsed IR light with an AFM tip in contact mode (**Figure 1**). PTIR has the advantage to be sensitive only to absorption, not to scattering, thus allowing materials identification and the direct comparison of the recorded spectra with FTIR libraries.^[16-18] Unlike FTIR, PTIR's lateral resolution for chemical imaging doesn't depend on the wavelength of light but depends on the tip size and on the sample's thermo-mechanical properties.^[19, 20] PTIR has been used for nanoscale chemical characterization of inhomogeneous samples such as bacteria,^[11, 15] polymers,^[17] embedded quantum dots^[21] and even living cells.^[22] It was assumed that the PTIR signal is proportional to absorption but this assumption has never been verified experimentally, nor has it been proved that PTIR can be used for quantitative chemical analysis at the nanoscale. The major goal of this paper is demonstrating that the PTIR signal is proportional to the absorbed energy, a necessary step towards the use of PTIR for nanoscale quantitative chemical characterization in disparate applications.

In this work, the lateral resolution, linearity and sensitivity of the PTIR technique was evaluated by measuring nano-patterned polymethylmethacrylate (PMMA) features fabricated on top of zinc selenide (ZnSe) prisms using electron beam lithography (EBL). Customized adaptor pieces were developed for a spinner and for the EBL tool to obtain lithographically nanofabricated patterns directly on the ZnSe prisms. Results shows that PTIR lateral resolution for chemical imaging is comparable to the lateral resolution obtained in the AFM height images, up to the smallest feature measured (100 nm). Spectra and chemical maps were produced from the thinnest sample analyzed (40 nm). Additionally, we demonstrate, for the

first time, that the intensity of the PTIR spectra of thin films ($< 1 \mu\text{m}$) depends linearly on the sample thickness which is a necessary requirement to use PTIR spectra and images for quantitative analysis at the nanoscale. Finally, by analyzing samples with an extended range of thicknesses we demonstrate experimentally that the PTIR intensity is proportional both to the local energy absorbed, to the thermal expansion and to persistence time of the thermal excitation in the sample as previously predicted theoretically.^[19]

2. Results and Discussion

PTIR requires a tunable pulsed laser source for sample illumination and an AFM tip in contact mode to measure the instantaneous thermal expansion induced by light absorption in the sample. The typical set up takes advantage of a total internal reflection configuration for illuminating the sample and minimizing the light-tip interaction which requires placing the sample over an optically transparent prism (**Figure 1a**). As the laser wavelength is tuned to match the sample's IR vibrational absorptions, the sample heats up, expands and deflects the AFM cantilever on a time scale much faster than the response of the AFM feedback. The instantaneous tip deflection is measured using a four-quadrant detector (**Figure 1a**) while the low repetition of the laser pulses (1 kHz) assures that the cantilever has enough time to complete the ring-down (**Figure 1b**) and that a new pulse will excite a sample and cantilever that have returned to equilibrium. The infrared spectrum of the sample is obtained by plotting the amplitude of the tip deflection with respect to the frequency.

The analysis of the PTIR signal is carried out either by determining the maximum of the deflection during the cantilever ring down (**Figure 1b**) or by determining the amplitude of one of the cantilever normal modes of vibration obtained by the Fourier transformation of the ring down signal (**Figure 1c**). Typically several pulses are averaged at each wavelength to increase the signal to noise ratio. A sample made of PMMA and Polystyrene (PS) particles embedded in an epoxy resin was prepared to illustrate the chemical specificity of the PTIR

signal. While the AFM height image alone (**Figure 2a**) doesn't allow phase identification, PTIR chemical image (**Figure 2b**) and spectra (**Figure 2c**) unambiguously allow identifying the composition of the different phases (see also **Figure S1** of the supporting information). The AFM height image and the PTIR chemical images in **Figure 2** were acquired simultaneously while illuminating the sample with the laser set at 1721 cm^{-1} , characteristic of the PMMA carboxylic groups,^[23] but not absorbed by PS or by the epoxy resin. It is clear that the AFM height images and the PTIR images carry different information. For example, extraneous particles (i.e. dust), observed in the height image (blue circles **Figure S2a**) of an EBL patterned PMMA sample (EBL-RP3), are not observed in the PTIR image (**Figure S2b**).

The samples analyzed here can be grouped into 2 categories: samples with constant thickness patterned with various features size and spacing (hereafter, resolution samples) used to assess the PTIR lateral resolution and samples with variable height patterned with lines (hereafter, wedged samples) to assess PTIR sensitivity and linearity. The spinner adaptor piece was designed to spin both flat thin films (center position in **Figure S3** of the supporting information) and wedged films by spinning the prisms at different angles (outermost positions on **Figure S3**).

The samples nanofabrication process is illustrated in **Figure 3** and **Figure S5** for the resolution and wedge sample, respectively (see experimental sections for details). Briefly, a PMMA positive EBL resist was spun on a prism and cured before depositing an aluminum layer, used to facilitate charge dissipation during the EBL process. The prism was then subjected to EBL using the aforementioned adaptor pieces (**Figure S4**) varying the electron beam dose depending on the type of pattern required. Finally, the aluminum layer was removed with a tetramethylammonium hydroxide water solution and the pattern was developed in a mixture of Methyl Iso-butylketone (MIBK) and IPA. Depending on the electron beam dose the PMMA film was patterned through the whole thickness (**Figure 3e**) or

partially (**Figure 3f**). PMMA wedged samples were prepared with a very similar process (see **Figure S5**) except that the prisms were spun at an angle and subsequently baked in an oven under vacuum using a tilted stage to avoid polymer flow that could occur at higher temperatures.

The AFM height image and the corresponding PTIR image of PMMA carboxylic groups (1720 cm^{-1}) of an EBL defined resolution sample (EBL-RP1) are compared in **Figure 4**. Both images were acquired simultaneously. The thickness of PMMA in EBL-RP1 is $300\text{ nm} \pm 10\text{ nm}$ while the pattern has features up to 130 nm high. The smallest feature in EBL-RP1 is approximately 200 nm wide, as determined from both the height and chemical image (**Figure 4**). The contrast in **figure 4d** is given by differences in the absorption intensity due to different sample thickness between the top ($\approx 300\text{ nm}$) and bottom ($\approx 170\text{ nm}$) of the lithographically defined features. The images were acquired with 25 nm pixel resolution and 64 pulses were averaged for each pixel.

In order to record a chemical image with the best lateral resolution, the AFM pixel per second (ξ_{AFM}) should be equal to the PTIR pixel per second (ξ_{PTIR}) defined as follows:

$$\xi_{AFM} = 2 \cdot n^{pixel} \cdot \nu \quad (2)$$

$$\xi_{PTIR} = \frac{\omega}{n^{avg-pulses}} \quad (3)$$

where n^{pixel} (pixel/line) is the number of pixel in the AFM scanning direction, ν is the AFM scan rate (lines/s), ω is the laser repetition rate (1 kHz in this work) and $n^{avg-pulses}$ is the number of pulses per pixel (typically from 16 to 64). If this condition is not met the pixel size of the PTIR chemical image will differ from the pixel size in the height image making correlations difficult if the two numbers are appreciably different.

A resolution sample (EBL-RP2) with a pattern developed through all the film thickness ($300 \text{ nm} \pm 10 \text{ nm}$) was analyzed. However, the smallest features in the sample were easily damaged by the AFM tip (see **Figure S6**). The correlation between the AFM height and the PTIR images (amplitude and peak) for the resolution samples is generally very good (see for example **Figure SN7**) and the lateral resolution in the images is comparable within the experimental limits ($\pm 10 \text{ nm}$), see **Figure 4**, **Figure S2** and **Figure S6**. The smallest feature measured in this work is $\approx 100 \text{ nm}$ as determined from both the height and chemical image in **Figure S6**. The ultimate PTIR lateral resolution lies below 100 nm but it could not be determined with the samples studied in this work. The PTIR image and spectrum of the thinnest sample analyzed ($40 \text{ nm} \pm 5 \text{ nm}$) is reported in the supporting information (**Figure S8**).

PTIR spectra obtained on patterned wedged samples with variable PMMA thickness (**Figure 5a**) were used to evaluate the linearity and sensitivity of the technique and to prove experimentally the dependence of the PTIR signal on sample thickness and optical constants. We provide here the first experimental demonstration that the PTIR signal is proportional to the energy absorbed (see below). **Figure 5b** shows that the PTIR signal increases linearly with thickness (z) for thicknesses up to $\sim 1 \text{ }\mu\text{m}$. The PTIR signal reaches a maximum (wavelength dependent) and then progressively decreases for thicker samples (**Figure 5c**). Below we show a simple model that describes well the PTIR signal trend versus thickness caused by the exponentially decaying field inside the sample due to the Attenuated Total Reflection (ATR) illumination geometry.

Dazzi et al. derived theoretically a complex expression for the PTIR signal.^[19, 20] The relevant conclusion of Dazzi's work for our purposes, i.e. the dependence of the PTIR signal from the sample thickness, is that, the signal is proportional to the sample thermal expansion, to the absorbed energy per unit area (U_{abs}) and, for short laser pulses, to the duration of the

thermal excitation (t_{relax}) in the sample. The sample thermal expansion is proportional to the sample thickness (z) while t_{relax} is approximately proportional to square of the sample thickness.^[19] Consequently, it is expected that the PTIR signal (S) should be proportional to:

$$S \sim U_{abs} \cdot z^3 \quad (4)$$

The ATR configuration and sample thicknesses used in this work combined with the relative strong absorption of PMMA^[24] void the small absorption approximation of the Lambert-Beer law previously used by Dazzi et al.^[19, 20] The absorption in the sample will depend on the evanescent decaying electric field intensity and will not be proportional to the sample thickness.

In ATR spectroscopy^[25] it is convenient to express the exponentially decaying evanescent field amplitude inside the sample in terms of penetration depth (d_p)

$$E = E_0 \cdot e^{-z/d_p} \quad (5)$$

Where E_0 is the electric field amplitude at the prism interface and d_p is the distance where E is reduced by a factor of e . It should be noted that the actual thickness sampled by the evanescent field is greater than d_p . The penetration depth depends on the wavelength (λ), the indexes of refraction of the not-absorbing ATR element (n_1) and of the sample ($\tilde{n}_2(\lambda) = n_2(\lambda) + i\kappa_2(\lambda)$) and the light angle of incidence:

$$d_p = \frac{\lambda}{2 \cdot \pi} \cdot \left[\frac{\sqrt{(n_1^2 \cdot \sin^2 \theta - n_2^2 + \kappa_2^2)^2 + (2 \cdot n_2 \cdot \kappa_2)^2} + (n_1^2 \cdot \sin^2 \theta - n_2^2 + \kappa_2^2)}{2} \right]^{-1/2} \quad (6)$$

Both the real part and the imaginary part of the refractive index change as a function of λ in proximity of the sample absorption peaks.^[24] This is particularly relevant for the strong absorption peaks characteristic of PMMA for which the influence of the extinction coefficient

on d_p cannot be neglected.^[24, 26] It should be noted that, contrary to the first PTIR reports,^[14] where light was transmitted through the sample and totally reflected at the sample-air interface, the experimental conditions used here ($\theta = 45^\circ$, $n_1 = 2.438$, $n_2(\lambda) = 1.2$ to 1.65 , $k_2(\lambda) = 0$ to 0.4)^[24] ensure that total internal reflection is achieved at all wavelengths (from 1800 cm^{-1} to 1200 cm^{-1}) at the prism-sample interface.

For not absorbing samples the expression of d_p is reduced to

$$d_p(k_2 = 0) = \frac{\lambda}{2 \cdot \pi \cdot n_1} \cdot \left[\sin^2 \theta - \left(\frac{n_2}{n_1} \right)^2 \right]^{-1/2} \quad (7)$$

Because of the conservation of energy we can express the absorbed energy per unit area by a sample as the difference between the evanescent fields intensities calculated for a non-absorbing medium and for a sample with extinction coefficient κ_2 :

$$U_{abs} \sim E_{k=0}^2 - E_{k=k_2}^2 \quad (8)$$

which is a non-monotonic function of z (**Figure S9**).

The experimental data fits well when substituting equation 8 into equation 4 (see **Figure 5c** and **Figure S10**). The penetration depth calculated by fitting the experimental data increases with wavelength as expected and was determined to be $1070 \text{ nm} \pm 9 \text{ nm}$, $1113 \text{ nm} \pm 12 \text{ nm}$ and $1160 \pm 9 \text{ nm}$ for the PMMA absorption peak at 1720 cm^{-1} , 1463 cm^{-1} and 1263 cm^{-1} , respectively. Our experiments prove that the PTIR theory developed by Dazzi et al.^[20] is fundamentally correct.

The linearity of the PTIR signal with thickness (**Figure. 5b**) is a very important result because it suggests that PTIR data could potentially be used for quantitative chemical analysis at the nanoscale for thin samples (z smaller than $\approx 1 \text{ }\mu\text{m}$). For this purpose one should link the PTIR signal to the concentration (C) but this task is hindered by the lack of a concentration

standard at the nanoscale. Since the PTIR signal is proportional to the absorbed energy and, under the conditions of validity of the Lambert and Beer approximation, the absorbance of a sample is proportional to its concentration, one should expect the PTIR signal to be proportional to concentration. This is valid for a mixture in which the two components have the same thermo-mechanical parameters. According to the theory proposed by Dazzi,^[20] the PTIR signal is proportional to the sample expansion coefficient (α) and inversely proportional to its thermal conductivity (k_{th}) which are included in the pre-factor of equation 4. For example, in first approximation the thermal conductivity for a mixture of 2 components (A, B) can be calculated as the weighted average of component's thermal conductivities:

$$k_{th}^{mix} = C_A \cdot k_{th}^A + (1 - C_A) \cdot k_{th}^B \quad (9)$$

Because the concentration of a component A determines both the absorbed energy and the thermo-mechanical properties of the mixture, we expect the PTIR signal to deviate from linearity if the components have significantly different thermo-mechanical properties. However, for mixtures of materials with similar thermo-mechanical properties such as some biological samples^[27] and polymers blends we expect this deviation to be small (see for example **Figure S11** of the supporting information).

3. Conclusions

In summary, the limits of PTIR technique were tested by analyzing nano-patterned polymer samples fabricated on unconventional 3-dimensional substrates. It was found that PTIR is a robust tool for simultaneous extraction of topological and chemical maps at the nanoscale. The samples developed in this work will be used in the future as benchmarks to assess the technique improvements. We have used a simple model and experimentally demonstrated for the first time that the PTIR signal is proportional to the energy absorbed and that the theory of

PTIR signal generation^[20] is correct. Arguably, the most relevant finding of this work is that for thin samples (z smaller than $\approx 1 \mu\text{m}$) the PTIR signal increases linearly as a function of sample thicknesses. This means that PTIR data could potentially be used for quantitative chemical analysis at the nanoscale impacting areas from material science to biology and medicine.

4. Experimental Section

All chemicals were used as received without further purification.

The spinner adaptor piece, made of polyphenylsulfone to ensure chemical compatibility with the EBL resist, was manufactured using Fused Deposition Modeling,^[28] a 3D printing technology.

Before spinning, the prisms were cleaned using oxygen plasma ash (1000 W, 15 min) and rinsed with acetone and isopropyl alcohol (IPA) to remove any impurities or dust particles adhering to the surface. In the case of the resolution samples (films with constant thickness) a PMMA positive EBL resist was spun at 33.3 Hz and baked in an oven at 140 °C for 30 min. Subsequently an aluminum layer of $\approx 30 \text{ nm}$ was deposited on top of the resist using an electron-beam evaporator for charge dissipation. The prism was then subjected to EBL varying the electron beam dose from $300 \mu\text{C}\cdot\text{cm}^{-2}$ to $700 \mu\text{C}\cdot\text{cm}^{-2}$ at 100 kV, depending on the type of pattern required. Finally, the aluminum layer was removed with a tetramethylammonium hydroxide water solution (2.4 % volume fraction) and the pattern was developed in a mixture of Methyl Iso-butylketone (MIBK) and IPA. The entire process is illustrated in **Figure 3**. PMMA wedged samples were prepared with a very similar process (see **Figure S5**) except that the prisms were spun at an angle and subsequently baked in an oven under vacuum ($\approx 133 \text{ Pa}$, 60 °C for 60 min) using a tilted stage to avoid polymer flow that could occur at higher temperatures. Additionally, after the initial cleaning, a piece of poly-4,4'-oxydiphenylene-pyromellitimide (POP) tape was applied to the prism top surface to

have the thinnest part of the wedge close to the center of the prism (**Figure S4**). The POP tape was removed before imaging the samples.

The PTIR instrument used in this work uses an optical parametric oscillator (OPO) laser with 1 kHz repetition rate and wavelength output tunable between 1200 cm^{-1} and 4000 cm^{-1} . PTIR spectra were recorded by averaging 4 consecutive spectra in the range between 1200 cm^{-1} and 1800 cm^{-1} . Each individual spectrum was recorded tuning the laser at 3 cm^{-1} interval and using 256 pulses per wavelength. PTIR images were recorded using the laser at a fixed wavelength by averaging from 16 to 64 pulses per pixel.

A least square method was used to estimate the penetration depth (dp) values fitting the experimental data. The method employs an iterative strategy to minimize the deviations of the theoretical curve from the experimental points based on the Levenberg-Marquardt algorithm.

Acknowledgements

The authors acknowledge Dr. Adrian Popescu of NIST for the help in fitting the data, Rich Kasica of NIST for useful discussion of EBL and Kevin Kjoller of Anasys Instruments for providing the microtomed sample. We thank Terry Raines, Dwight Barry and John Kisner of the NIST machine shop. A. C. acknowledges support from the National Institute of Standards and Technology American Recovery and Reinvestment Act Measurement Science and Engineering Fellowship Program, Award 70NANB10H026, through the University of Maryland.

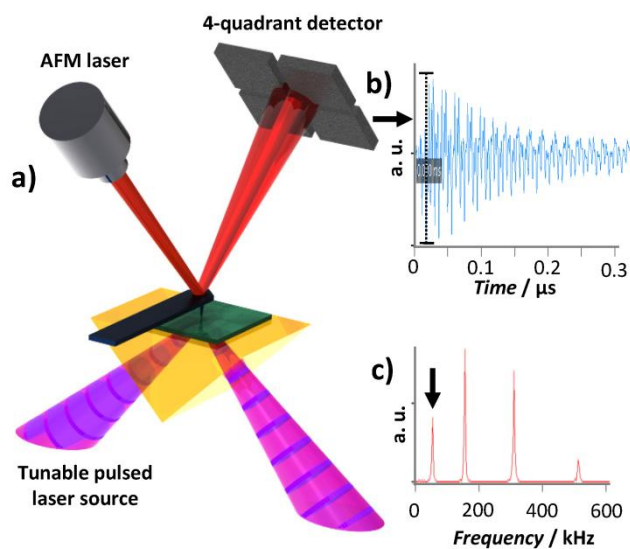


Figure 1. a) Schematic of the PTIR set up: if the IR laser pulses (purple) are absorbed by the sample (green) it rapidly expands and deflects the AFM cantilever; the amplitude of the deflection, which is proportional to the energy absorbed, is measured by the AFM four-quadrant detector. The PTIR signal analysis is carried out either by (b) determining the maximum of peak to peak deflection during the cantilever ring down (blue signal) or by (c) Fourier transformation determining the amplitude of one of the cantilever normal modes of vibration (red signal).

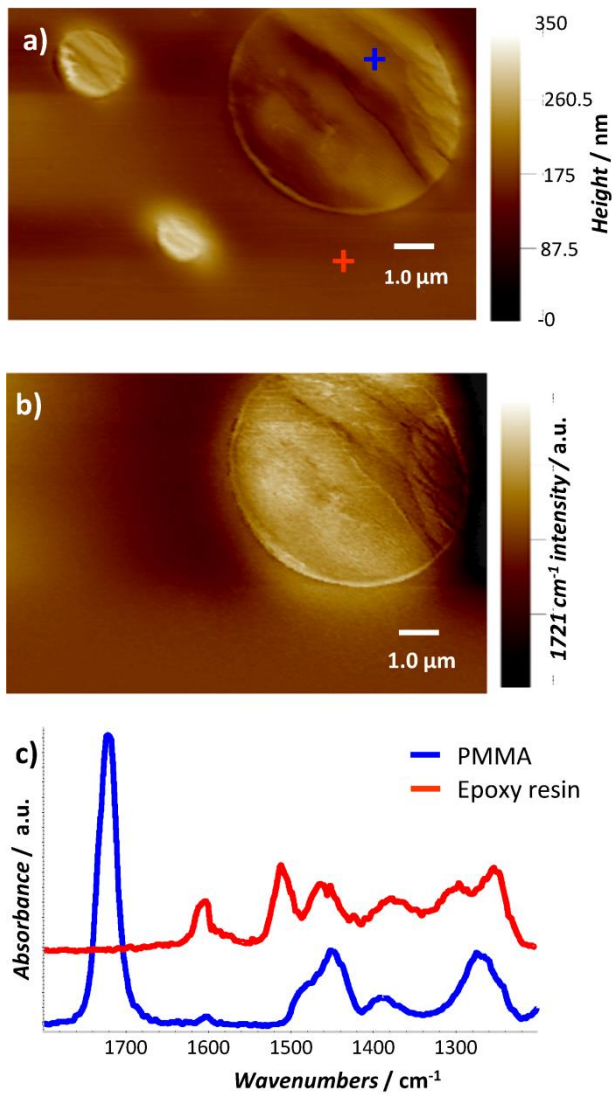


Figure 2. a) AFM height image showing a PMMA particle (large) and 2 PS particles (small) embedded in epoxy resin, b) simultaneous PTIR chemical image obtained pulsing the IR laser at 1721 cm^{-1} a frequency characteristic of the carboxylic groups of PMMA; the PTIR image allows to identify the chemical composition of the different phases in the sample. c) PTIR spectra of PMMA (blue) and epoxy resin (red) obtained from the selected locations (red and blue +) in figure 2a.

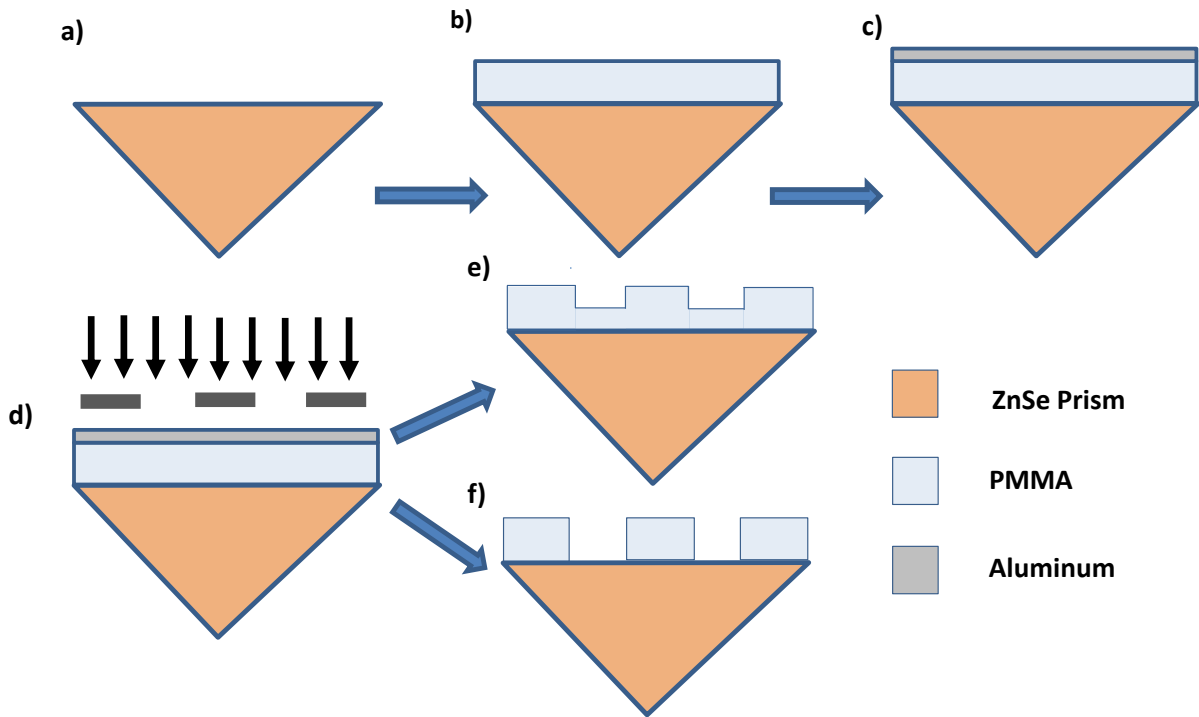


Figure 3. Nanofabrication schematic of PMMA resolution samples on ZnSe prisms: a) prism cleaning, b) PMMA spinning, c) aluminum charge dissipation layer deposition, d) Electron Beam Lithography process, e, f) aluminum layer removal and PMMA development; the height of the patterned features is a function of the electron beam dose used.

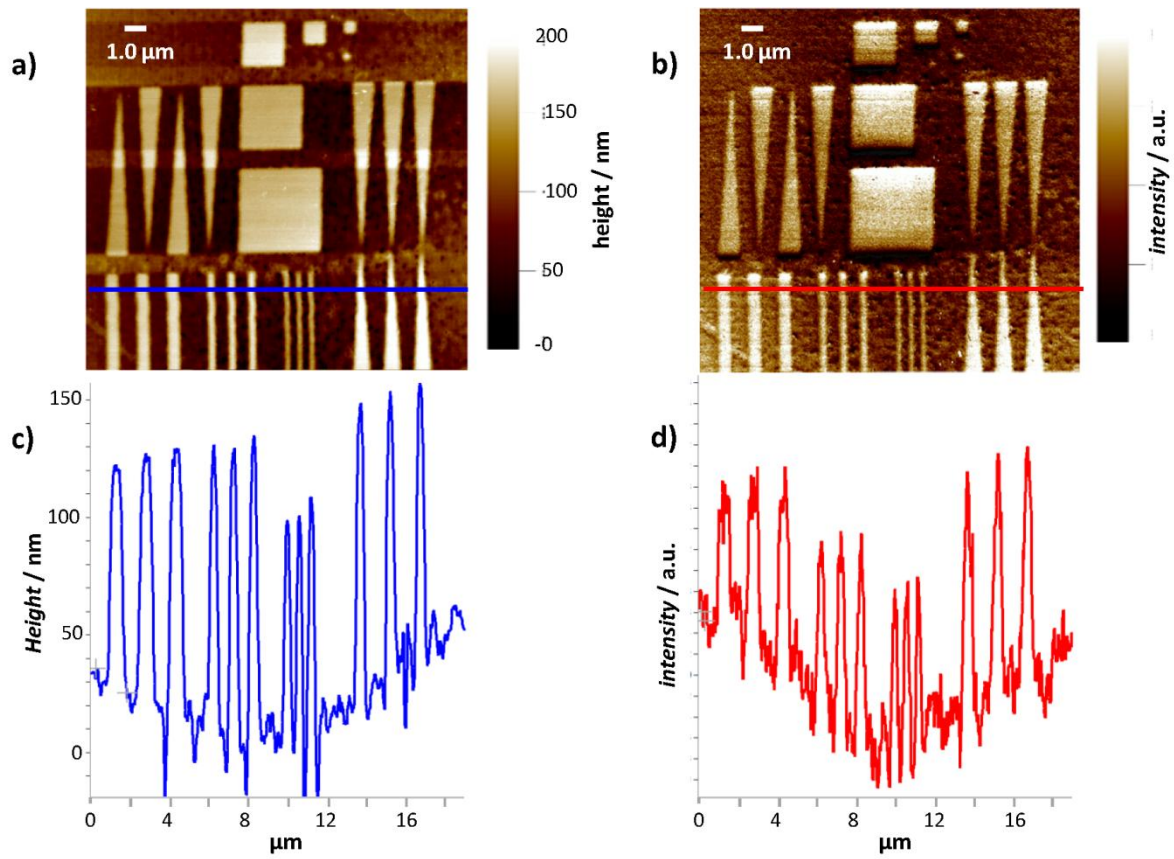


Figure 4. PMMA patterned sample (EBL-RP1): a) AFM height image, b) PTIR chemical image (peak signal) recorded obtained pulsing the IR laser at 1720 cm^{-1} characteristic of the PMMA carboxylic group, c) representative line scan from the height image in figure 3a (blue), d) representative line scan from the PTIR chemical image in figure 3b (red).

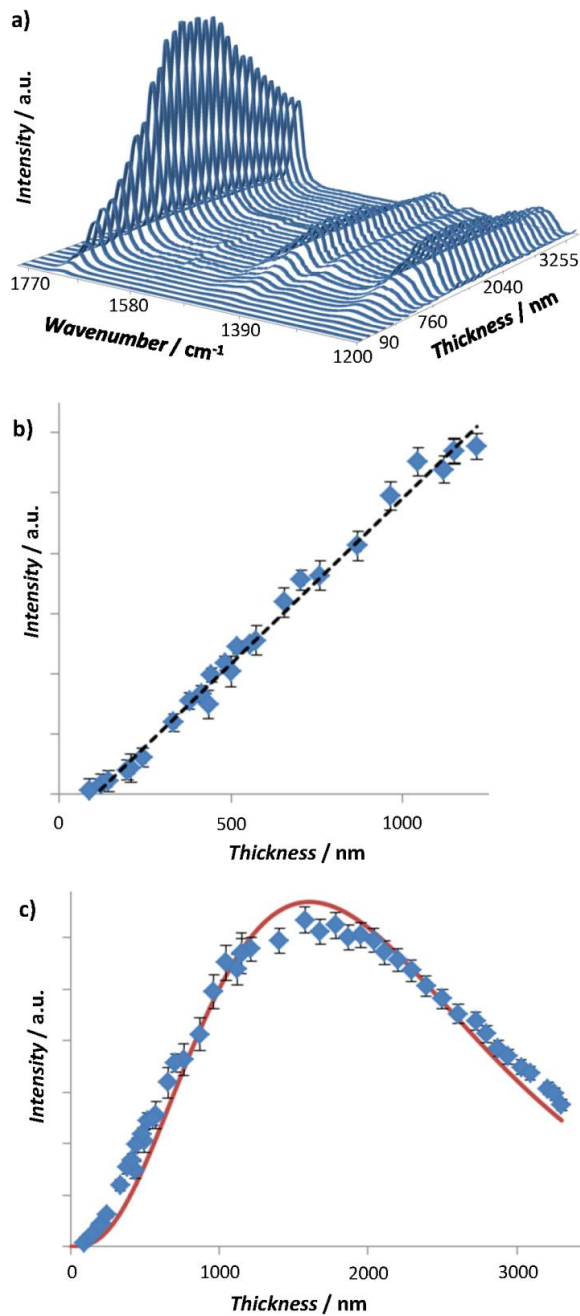


Figure 5. a) PTIR spectra intensity of PMMA as a function of thickness. b) Intensity of the 1720 cm^{-1} PMMA peak as a function of thickness; linear interpolation has a correlation coefficient (R^2) of 0.993 for thicknesses up to 1200 nm. c) Intensity of the 1720 cm^{-1} PMMA peak as a function of thickness for thicknesses up to 3300 nm; experimental data are interpolated by the function $\alpha \cdot z^3 \cdot e^{-2 \cdot \frac{z}{d_p}}$ with $R^2=0.963$ and $d_p=1070\text{ nm} \pm 9\text{ nm}$. The horizontal error bars, which are smaller than the dots size, represent a single standard

deviation in the AFM height measure. The vertical error bars represent a single standard deviation in the integration of the PTIR lines.

- [1] a) D. G. Cahill, W. K. Ford, K. E. Goodson, G. D. Mahan, A. Majumdar, H. J. Maris, R. Merlin, Phillipot, Sr., *J. Appl. Phys.* **2003**, *93*, 793; b) A. Centrone, E. Penzo, M. Sharma, J. W. Myerson, A. M. Jackson, N. Marzari, F. Stellacci, *Proc. Nat. Acad. Sci U.S.A.* **2008**, *105*, 9886; c) M. A. El-Sayed, *Acc. Chem. Res.* **2001**, *34*, 257.
- [2] L. J. Zhang, T. J. Webster, *Nano Today* **2009**, *4*, 66.
- [3] A. J. Huber, J. Wittborn, R. Hillenbrand, *Nanotechnology* **2010**, *21*, 235702.
- [4] P. G. Nicholson, F. A. Castro, *Nanotechnology* **2010**, *21*, 492001.
- [5] D. C. Fernandez, R. Bhargava, S. M. Hewitt, I. W. Levin, *Nat. Biotechnol.* **2005**, *23*, 469.
- [6] J. H. Park, G. von Maltzahn, L. Ong., A. Centrone, T. A. Hatton, E. Ruoslahti, S. N. Bhatia, M. J. Sailor, *Adv. Mater.* **2009**, *22*, 880.
- [7] a) A. Centrone, Y. Hu, A. M. Jackson, G. Zerbi, F. Stellacci, *Small* **2007**, *3*, 814; b) G. R. Rao, C. Castiglioni, M. Gussoni, G. Zerbi, E. Martuscelli, *Polymer* **1985**, *26*, 811.
- [8] a) C. Petibois, M. Piccinini, M. C. Guidi, A. Marcelli, *J. Synchrotron Radiat.* **2010**, *17*, 1; b) M. J. Nasse, M. J. Walsh, E. C. Mattson, R. Reininger, A. Kajdacsy-Balla, V. Macias, R. Bhargava, C. J. Hirschmugl, *Nat. Methods* **2011**, *8*, 413.
- [9] B. Knoll, F. Keilmann, *Nature* **1999**, *399*, 134.
- [10] a) R. Hillenbrand, T. Taubner, F. Keilmann, *Nature* **2002**, *418*, 159; C. b) A. Michaels, S. J. Stranick, L. J. Richter, R. R. Cavanagh, *J. Appl. Phys.* **2000**, *88*, 4832; c) L. Bozec, A. Hammiche, H. M. Pollock, M. Conroy, J. M. Chalmers, N. J. Everall, L. Turin, *J. Appl. Phys.* **2001**, *90*, 5159; d) L. Bozec, A. Hammiche, M. J. Tobin, J. M. Chalmers, N. J. Everall, H. M. Pollock, *Meas. Sci. Technol.* **2002**, *13*, 1217.
- [11] A. Dazzi, R. Prazeres, F. Glotin, J. M. Ortega, *Ultramicroscopy* **2007**, *107*, 1194.
- [12] M. Brehm, T. Taubner, R. Hillenbrand, F. Keilmann, *Nano Lett.* **2006**, *6*, 1307.
- [13] a) B. Knoll, F. Keilmann, *Opt. Commun.* **2000**, *182*, 321; b) A. Cvitkovic, N. Ocelic, R. Hillenbrand, *Opt. Express* **2007**, *15*, 8550.
- [14] A. Dazzi, R. Prazeres, E. Glotin, J. M. Ortega, *Opt. Lett.* **2005**, *30*, 2388.
- [15] A. Dazzi, R. Prazeres, F. Glotin, J. M. Ortega, M. Al-Sawaftah, M. de Frutos, *Ultramicroscopy* **2008**, *108*, 635.
- [16] C. Mayet, A. Dazzi, R. Prazeres, J. M. Ortega, D. Jaillard, *Analyst* **2010**, *135*, 2540.
- [17] C. Marcott, M. Lo, K. Kjoller, C. Prater, I. Noda, *Appl. Spectrosc.* **2011**, *65*, 1145.
- [18] K. Kjoller, J. R. Felts, D. Cook, C. B. Prater, W. P. King, *Nanotechnology* **2010**, *21*, . 185705
- [19] A. Dazzi, in *Thermal Nanosystems and Nanomaterials*, Vol. 118 (Ed: S. Volz), **2009**, 469.
- [20] A. Dazzi, F. Glotin, R. Carminati, *J. Appl. Phys.* **2010**, *107*, 124519.
- [21] S. Sauvage, A. Driss, F. Reveret, P. Boucaud, A. Dazzi, R. Prazeres, F. Glotin, J. M. Ortega, A. Miard, Y. Halioua, F. Raineri, I. Sagnes, A. Lemaitre, *Phys. Rev. B* **2011**, *83*, 035302.
- [22] C. Mayet, A. Dazzi, R. Prazeres, E. Allot, E. Glotin, J. M. Ortega, *Opt. Lett.* **2008**, *33*, 1611.
- [23] L. J. Bellamy, *The Infrared Spectra of Complex Molecules*, New York **1980**.
- [24] R. T. Graf, J. L. Koenig, H. Ishida, *Appl. Spectrosc.* **1985**, *39*, 405.
- [25] a) N. J. Harrick, *Internal Reflection Spectroscopy*, Interscience Publisher, New York **1967**; b) H. Hosono, *J. Appl. Phys.* **1991**, *69*, 8079.

- [26] L. A. Averett, P. R. Griffiths, K. Hishikida, *Anal. Chem.* **2008**, *80*, 3045.
[27] J. W. Valvano, J. R. Cochran, K. R. Diller, *Int. J. Thermophys.* **1985**, *6*, 301.
[28] I. Zein, D. W. Hutmacher, K. C. Tan, S. H. Teoh, *Biomaterials* **2002**, *23*, 1169.

Supporting information for:

Chemical Imaging Beyond the Diffraction Limit: Experimental Validation of the PTIR Technique **

Basudev Lahiri,^{1,2} Glenn Holland¹ and Andrea Centrone^{1,2}*

[*] Dr. Andrea Centrone, Dr. Basudev Lahiri,

¹NIST, Center for Nanoscale Science and Technology
Gaithersburg, 100 Bureau Drive, Stop 6204, MD 20899 (USA)

²University of Maryland, Institute for Research in Electronics and Applied Physics (IREAP),
College Park, MD 20742 (USA)

E-mail: Andrea.Centrone@nist.gov

Mr. Glenn Holland

¹NIST, Center for Nanoscale Science and Technology
Gaithersburg, 100 Bureau Drive, Stop 6204, MD 20899 (USA)

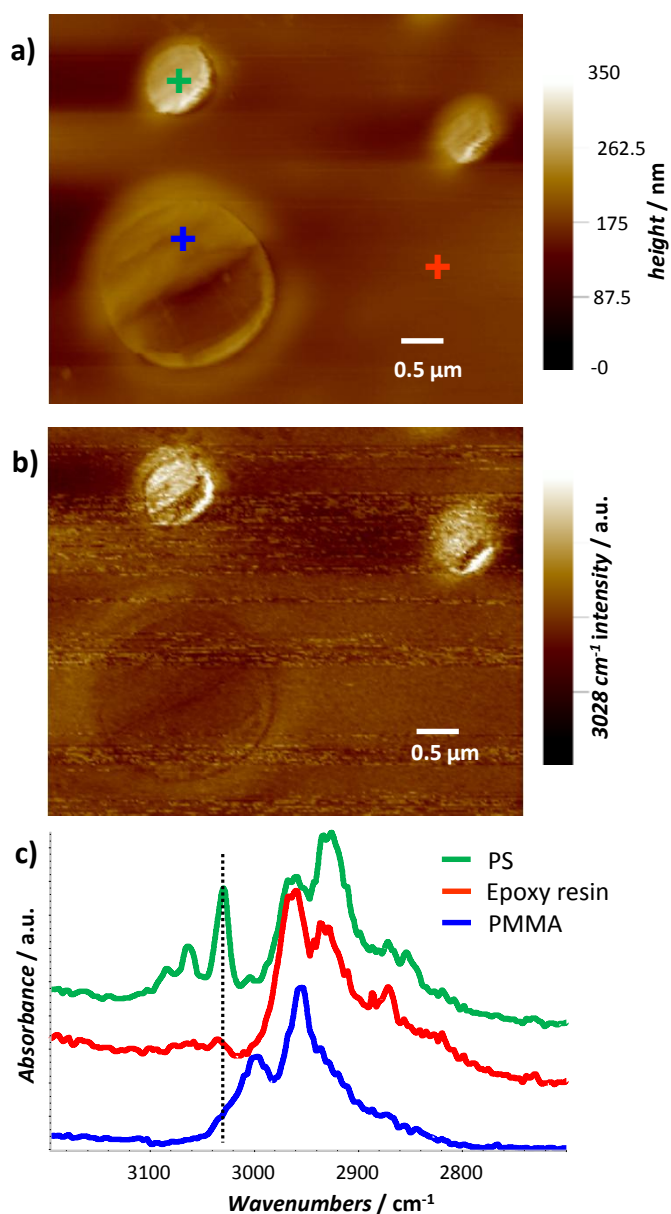


Figure S1. a) AFM height image showing a PMMA particle (large) and 2 PS particles (small) embedded in epoxy resin, b) simultaneous PTIR chemical image obtained tuning the laser at 3028 cm^{-1} a frequency characteristic of the aromatic CH stretching of PS, c) PTIR spectra of PMMA (blue), epoxy resin (red) and PS (green), obtained from the selected locations (+) in fig. S1a.

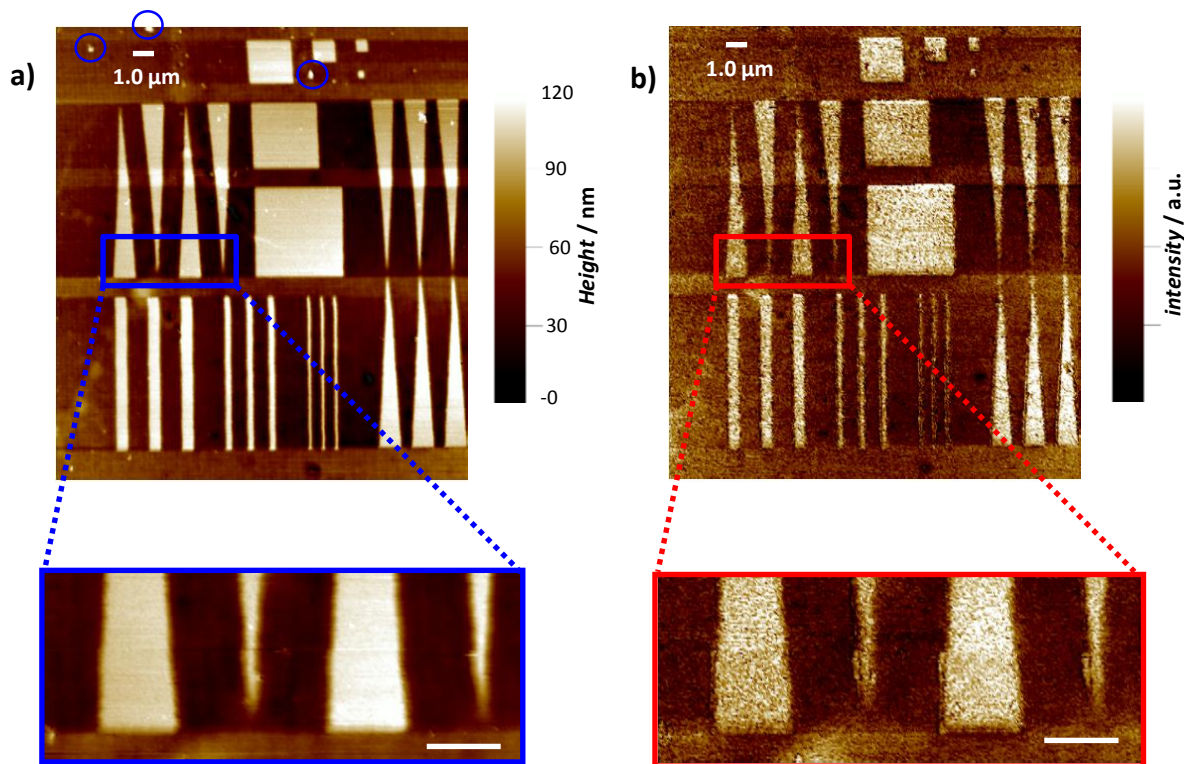


Figure S2. a) AFM height image and b) corresponding PTIR chemical image (amplitude signal at 1720 cm^{-1}) of a PMMA patterned sample (EBL-RP3); the film thickness is $290\text{ nm} \pm 10\text{ nm}$ and the patterned features are $\approx 85\text{ nm}$ tall. The scale bar in the insets is $1\text{ }\mu\text{m}$. A few small features (attributed to dust particles extraneous to the sample) observed in the height image (blue circles) but don't appear in the chemical image.

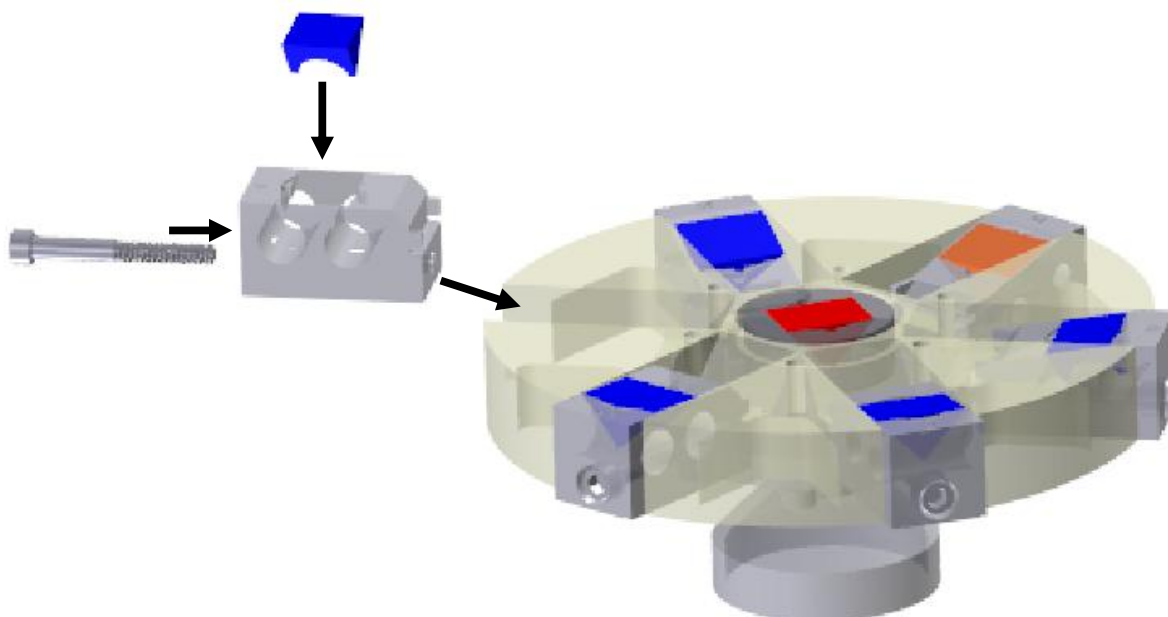


Figure S3. 3D drawing of the adaptor used to spin ZnSe prisms at 33.3 Hz. The prism is placed in the central position (red) for spinning film with constant thickness. Each one of the removable inserts (grey) allows spinning a prism (orange) at an angle (1° , 2° , 5° , 10° , 15° and 20°). Typically, only 1 prism is spun at a time and, to assure smooth operation, 5 calibrated brass counterweights (blue) are used. Since brass is denser than ZnSe the brass counterweights were machined to match the weight of the ZnSe prisms.

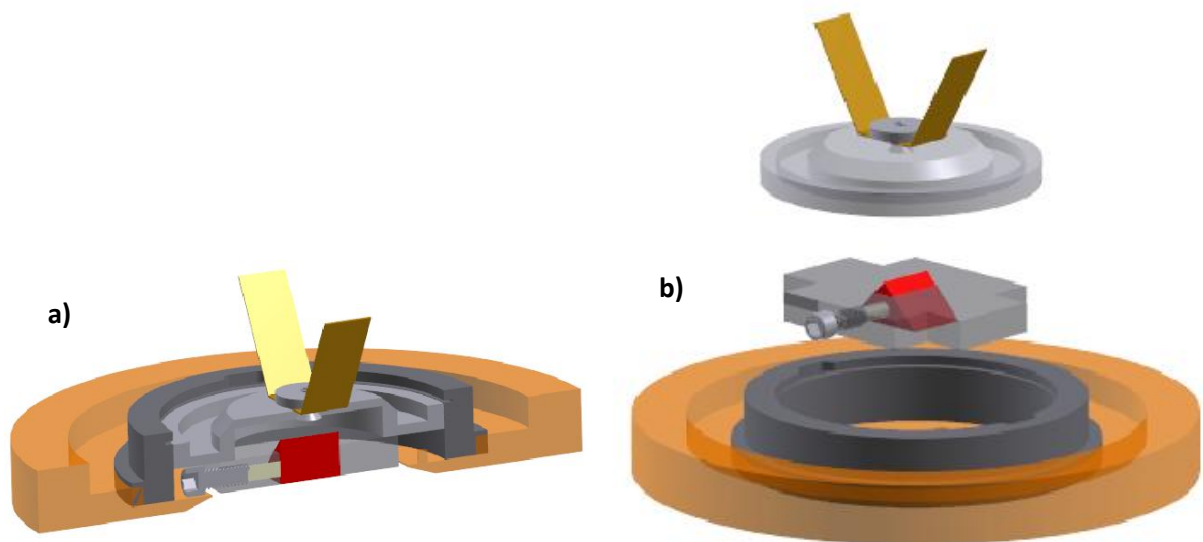


Figure S4. 3D drawing of the custom adaptor pieces (light gray pieces) used for mounting a ZnSe prism (red) on an electron beam lithography cassette originally designed to hold flat wafers (orange and dark gray pieces): a) assembled section view, b) “exploded view”.

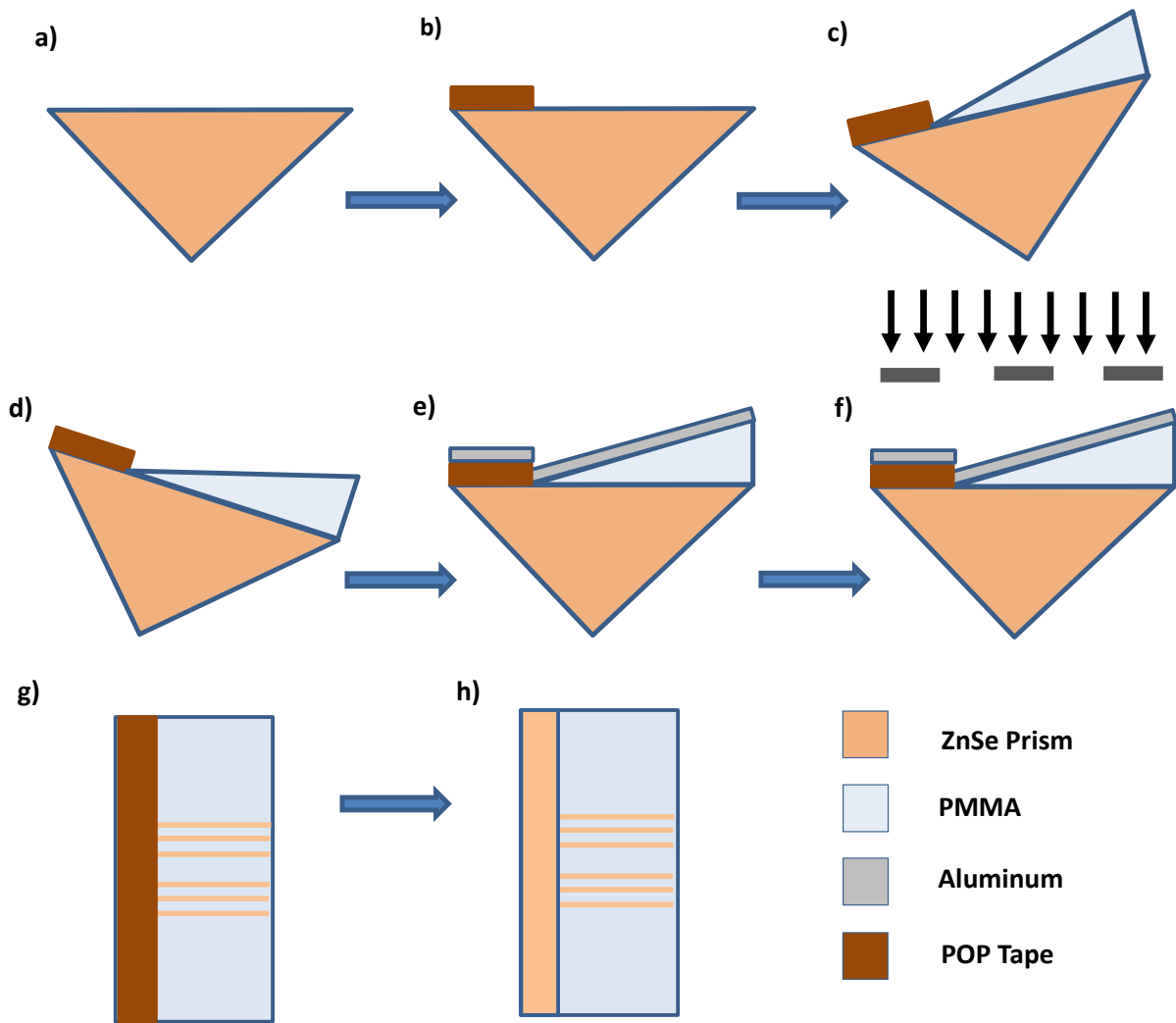


Figure S5. Nanofabrication schematic of PMMA wedged samples on ZnSe prisms: a) prism cleaning, b) poly-4,4'-oxydiphenylene-pyromellitimide (POP) tape application, c) PMMA spinning at an angle, d) substrate baking under vacuum with a tilt to avoid PMMA flow, e) aluminum charge dissipation layer deposition, f) Electron Beam Lithography process, g) aluminum layer removal and PMMA development to obtain the desired pattern (top view), h) POP tape removal (top view).

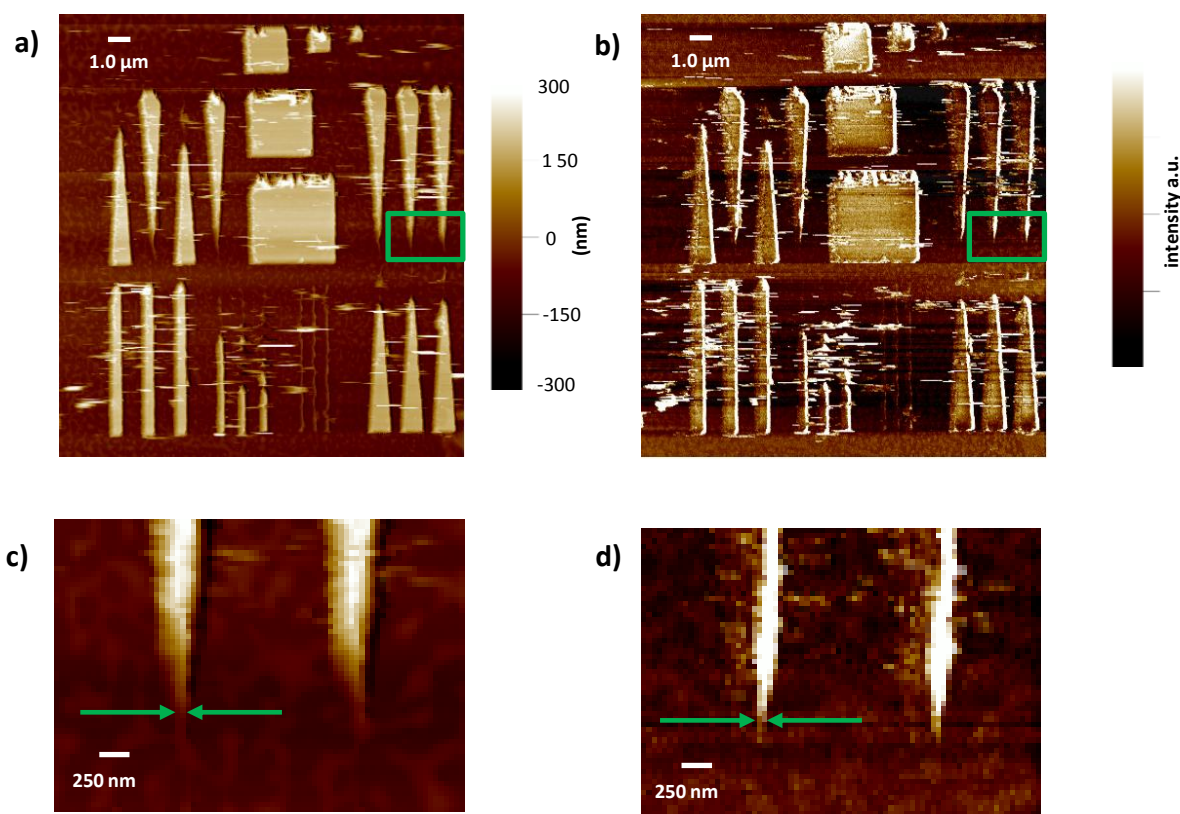


Figure S6. PMMA patterned sample (EBL-RP2): a) AFM height image, b) PTIR chemical image (peak signal) obtained pulsing the IR laser at 1720 cm^{-1} corresponding to the absorption of the PMMA carboxylic groups. The patterned features are $\approx 300\text{ nm}$ tall and were easily damaged by the AFM tip during the scanning. The lateral deflection of the tip causes dark edges in the height image and bright edges in the PTIR image. The smallest feature measured in EBL-RP2 (identified by green arrows) is approximately 100 nm wide, as determined from both the height (c) and PTIR chemical image (d).

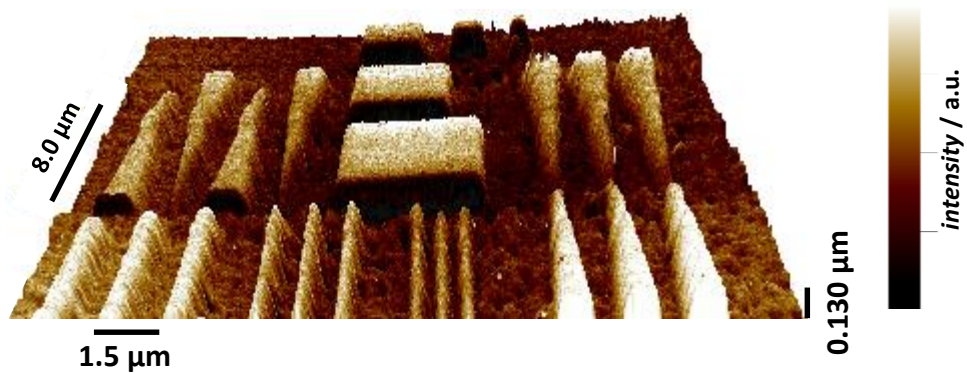


Figure S7. 3D Overlay of the PTIR chemical image (peak signal) and AFM height image of PMMA patterned sample EBL-RP1. The PTIR data were obtained at 1720 cm^{-1} characteristic of the PMMA carboxylic group. The z axis represents the thickness of the AFM image (see fig. 4a of the main text) while the color code represents the intensity of the PTIR signal (see fig. 4b).

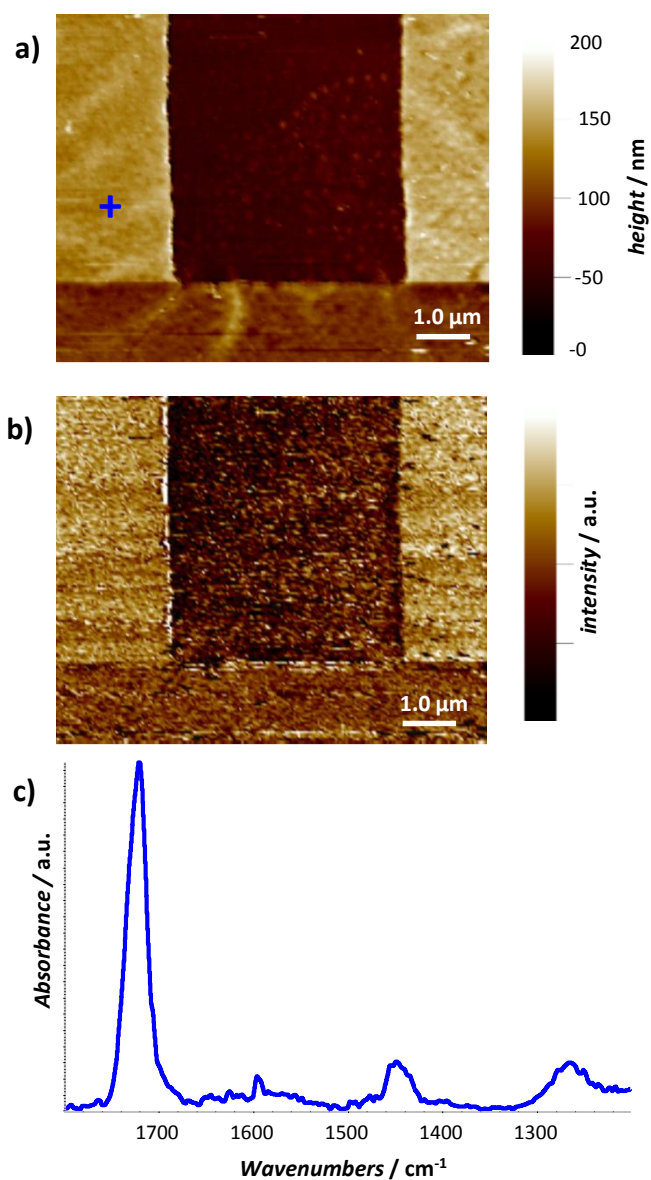


Figure S8. AFM height image (a) and PTIR chemical image (b, amplitude signal) of the thinnest sample analyzed in this work ($40 \text{ nm} \pm 5 \text{ nm}$) recorded setting the laser wavelength to 1720 cm^{-1} characteristic of the PMMA carboxylic group. PTIR spectra of PMMA (c) obtained from the marked location (+) in fig. S8a.

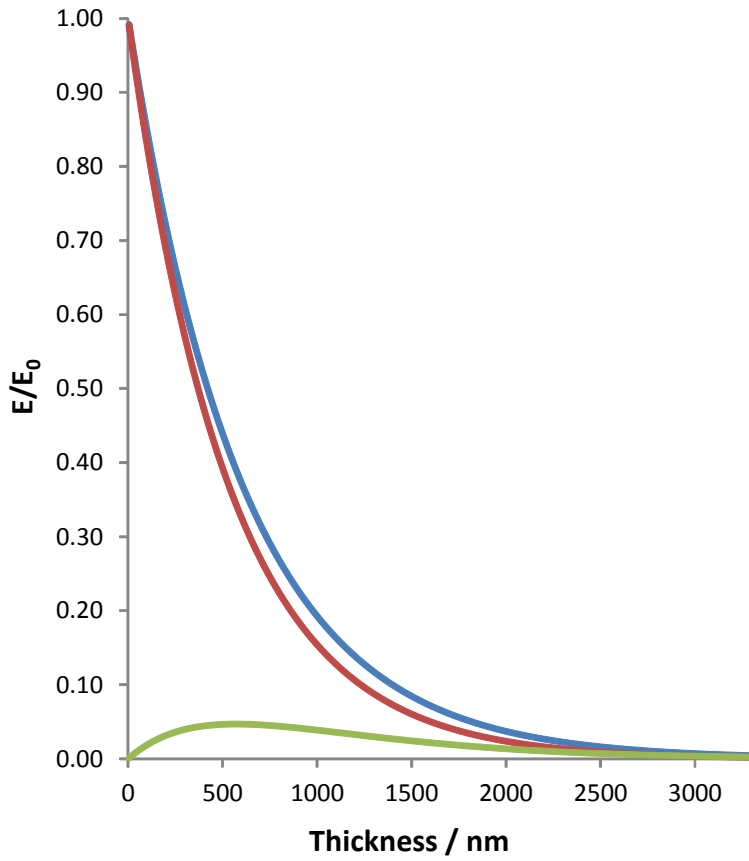


Figure S9. Calculated Electric evanescent electric field intensity ($\lambda = 1720 \text{ cm}^{-1}$, $\theta = 45^\circ$ and $n_{\text{ZnSe}} = 2.438$ in the case of a not absorbing medium (blue, $n_{\text{PMMA}} = 1.54$, $k_2 = 0$) and in the case of PMMA (red, $n_{\text{PMMA}} = 1.54$, $k_{\text{PMMA}} = 0.2$). The calculated absorbed energy as a function of thickness according equation 7 in the main text is shown in green.

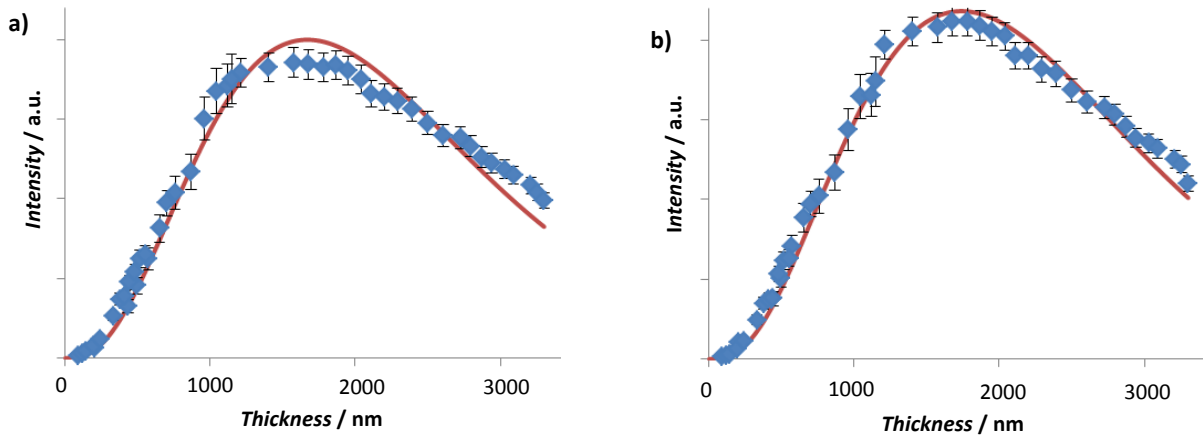


Figure S10. a) Intensity of the 1463 cm^{-1} PMMA peak as a function of thickness; experimental data are interpolated by the function $\alpha \cdot z^3 \cdot e^{-2 \cdot \frac{z}{d_p}}$ with $R^2 = 0.969$ and $d_p = 1113\text{ nm} \pm 12\text{ nm}$. b) Intensity of the 1263 cm^{-1} PMMA peak as a function of thickness; experimental data are interpolated by the function $\alpha \cdot z^3 \cdot e^{-2 \cdot \frac{z}{d_p}}$ with $R^2=0.985$ and $d_p = 1160\text{ nm} \pm 9\text{ nm}$. The horizontal error bars, which are smaller than the dot size, represent a single standard deviation in the AFM height measure. The vertical error bars represent a single standard deviation in the integration of the PTIR lines.

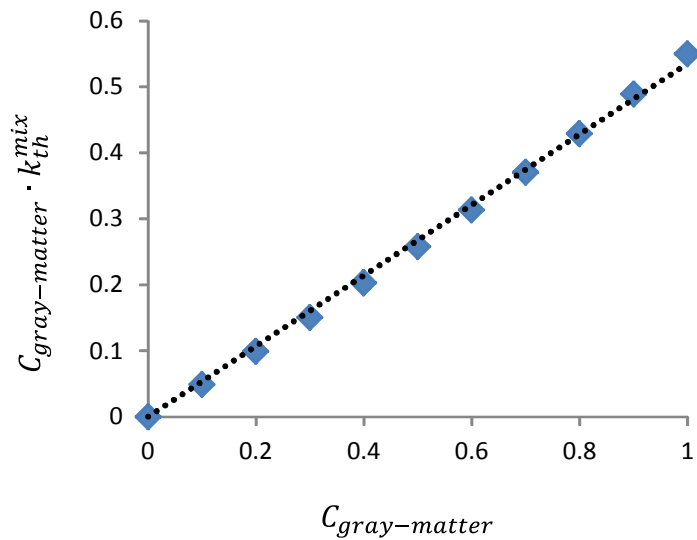


Figure S11. Calculated product between the brain gray matter concentration (C_{gray_matter}) and the thermal conductivity (calculated using equation 9 in the main text) for hypothetical brain grey and white matter mixtures. The values of the thermal conductivity used for the calculations were $0.55 \text{ W}\cdot\text{m}^{-1}\cdot\text{K}^{-1}$ and $0.48 \text{ W}\cdot\text{m}^{-1}\cdot\text{K}^{-1}$ for brain gray matter and white matter respectively (<http://www.itis.ethz.ch/itis-for-health/tissue-properties/database/thermal-conductivity/>). The calculated values can be interpolated with a linear function with correlation coefficient $R^2=0.9977$.